Title: Spectral Scanning and Fluorescence Lifetime Imaging Microscopy (FLIM) Enable Separation and Characterization of *C. elegans* Autofluorescence in the Cuticle and Gut

Running title: *C.elegans* autofluorescence analysis

Authors: Heino J. Hulsey-Vincent, Elizabeth A. Cameron, Caroline L. Dahlberg, Domenico F. Galati

Key words: *C. elegans*, autofluorescence, GFP, FLIM, spectral, gut granules

Abstract:

C. elegans gut and cuticle produce a disruptive amount of autofluorescence during imaging. Although *C. elegans* autofluorescence has been characterized, it has not been characterized at high resolution using both spectral and fluorescence lifetime-based approaches. We performed high resolution spectral scans of whole, living animals to characterize autofluorescence of adult *C. elegans*. By scanning animals at 405 nm, 473 nm, 561 nm, and 647 nm excitations, we produced spectral profiles that confirm the brightest autofluorescence has a clear spectral overlap with the emission of green fluorescent protein (GFP). We then used Fluorescence Lifetime Imaging Microscopy (FLIM) to further characterize autofluorescence in the cuticle and the gut. Using FLIM, we were able to isolate and quantify dim GFP signal within the sensory cilia of a single pair of neurons that is often obscured by cuticle autofluorescence. In the gut, we found distinct spectral populations of autofluorescence that could be excited by 405 nm and 473 nm lasers. Further, we found lifetime differences between subregions of this autofluorescence when stimulated at 473 nm. Our results suggest that FLIM can be used to differentiate biochemically unique populations of gut autofluorescence without labeling. Further studies involving *C. elegans* may benefit from combining high resolution spectral and lifetime imaging to isolate fluorescent protein signal that is mixed with background autofluorescence and to perform useful characterization of subcellular structures in a label-free manner.

Introduction:

The model organism, *Caenorhabditis elegans (C. elegans),* is a transparent nematode that is amenable to microscopy and study through live imaging. *C. elegans* imaging often uses fluorescence to analyze promoter reporters, fusion proteins or dyes that label subcellular

structures (Corsi et al., 2015; El Mouridi et al., 2022; Mendoza et al., 2024; Yemini et al., 2021). Fluorescence imaging of *C. elegans* is central to diverse research questions from developmental biology to behavioral neurobiology (Bao et al., 2006; Chung et al., 2013; Tian et al., 2009). However, fluorescence imaging in *C. elegans* must contend with autofluorescence emitted from tissues and materials, such as a protective cuticle and intestinal lysosome-related organelles (gut granules) (Hermann et al., 2005; Pincus et al., 2016; A. C. Teuscher & Ewald, 2018). This was observed as early as the first account of *C. elegans* expressing GFP, where autofluorescence was noted to obscure the GFP signal (Chalfie et al., 1994). Methods that overcome autofluorescence in *C. elegans* will remove barriers to fluorescence imaging in live animals. This is especially true in areas and tissues where autofluorescence is particularly strong, such as the gut and cuticle (Heppert et al., 2016; Komura et al., 2021a; Pincus et al., 2016).

Spectral approaches are a common way to overcome *C. elegans* autofluorescence. For example, carefully chosen bandpass filters can partially separate autofluorescence emission from GFP emission in the gut (Morris et al., 2018), intensity-based autofluorescence correction can improve the GFP signal to noise ratio in the developing embryo (Rodrigues et al., 2022), and spectral unmixing can separate fluorescent protein emission from autofluorescence (Jones & Ashrafi, 2009). Alternatively, one can rationally choose fluorescent proteins that have minimal spectral overlap with autofluorescence (Heppert et al., 2016; Thomas et al., 2019) or use non-genetically encoded fluorescent probes that emit in the infra-red range (Hendler-Neumark et al., 2021; Rashtchian et al., 2021). Finally, studies have used the genetic power of *C. elegans* to remove the source of autofluorescence by performing experiments in backgrounds that do not produce autofluorescent gut granules (Eichel et al., 2022).

An additional parameter that can differentiate spectrally similar fluorophores is fluorescence lifetime, which is the temporal delay between the arrival of an excitation photon and the generation of an emission photon. Each fluorophore has a unique fluorescence lifetime that depends upon the chemical structure of the fluorophore and the environment (i.e., solvent) that surrounds the fluorophore (as reviewed in Datta et al., 2020). Fluorescence lifetime can be imaged with Fluorescence Lifetime Imaging Microscopy (FLIM) and quantified through curve fitting or phasor analysis (Phasor-FLIM). Although curve fitting is widely accepted, this approach requires pre-existing knowledge about the decay parameters of the fluorophores that are being analyzed. In contrast, Phasor-FLIM analysis does not make any assumptions about the

underlying decay parameters of fluorophores (as reviewed in Malacrida et al., 2021). Phasor-FLIM has been used to quantify NADH/NAD(P)H and FAD/$FADH_2$ ratios in metabolic studies (Bhattacharjee et al., 2017; Ma et al., 2016), separate spectrally similar fluorophores (Gonzalez Pisfil et al., 2022), distinguish known fluorophores from autofluorescence (Szmacinski et al., 2014), and quantify fluorescence resonance energy transfer (FRET) efficiency of fluorescent proteins (Lou et al., 2019). In *C. elegans*, FLIM has been used to investigate protein-protein interactions (Gallrein et al., 2021; Laine et al., 2019; Llères et al., 2017) and environmental effects on metabolic dyes (W.-W. Chen et al., 2023). However, these studies do not address native autofluorescence in *C. elegans*, which has both biological relevance and a long history of complicating fluorescent protein quantification.

In this study, we performed a systematic analysis of the spectral and lifetime properties of *C. elegans* autofluorescence relative to the emission profiles of conventional fluorophores, such as GFP and mCherry. We show that dim GFP fluorescence can be reliably separated from bright cuticle autofluorescence using Phasor-FLIM. We also demonstrate that spectrally similar gut autofluorescence can be characterized in a label-free manner by capitalizing on heterogeneous lifetimes.

Results and Discussion:

To determine the autofluorescence spectrum of live *C. elegans*, young adult animals were stimulated with four common excitation lines (405 nm (BFP/DAPI), 473 nm (GFP), 561 nm (mCherry), and 647 nm (emiRFP670/Alexa 647)) and non-overlapping 30 nm emission bins were collected across the entire visible and near infrared spectrum (Figure 1A and B, Supplemental Figure 1). To quantify the spectral data, the mean pixel intensity for each emission bin was calculated across the entire animal and plotted as a spectral profile (Figure 1C and D). In agreement with other findings (Heppert et al., 2016; Hermann et al., 2005), this approach revealed that 405 nm and 473 nm excitation stimulate autofluorescence with strong emission in the 450-600 nm range (Figure 1B and 1D). Conversely, 561 nm excitation stimulates autofluorescence with weak emission in the 570-720 nm range, and 647 nm excitation produces little to no emission (Figure 1B and 1D). To assess the variability of the spectral profiles, we collected data from 5 separate animals. We found that 405 nm and 473 nm excitation consistently stimulate strong emission (Supplemental Figure 2A-E), while 561 nm excitation produced weak and variable emission that ranged from barely detectable

(Supplemental Figure 2A-C) to undetectable (Supplemental Figure 2D and E). Anatomically, the strongest autofluorescence was observed in the gut (Figure 1B asterisk) and cuticle (Figure 1B box and arrowhead). These results demonstrate that *C. elegans* produce a wide spectrum of autofluorescence that is distributed throughout the body of the animal, and the most intense emission overlaps with commonly used green fluorescent proteins and dyes.

Our spectral analysis agrees with the well-documented interference from autofluorescence in the *C. elegans* gut and the cuticle, which can make it difficult to quantify weak GFP signals (Chalfie et al., 1994; Hermann et al., 2005; Monici, 2005; Morris et al., 2018; Pincus et al., 2016; A. C. Teuscher & Ewald, 2018). Although the GFP and autofluorescence spectra overlap, we hypothesized that their lifetimes could be resolved, which would allow GFP intensity to be measured even in the presence of background autofluorescence. To test this possibility, we imaged animals expressing P*odr-10::ODR-10::GFP*, which is an odorant receptor protein that localizes to ciliated sensory neurons at the anterior end of the animal (Ryan et al., 2014; Sengupta et al., 1996). Regardless of the presence of the fluorescent transgene, we found that excitation using the 473 nm laser led to cuticle autofluorescence (Figure 2A, magenta arrowhead). In animals with high levels of ODR-10::GFP expression, the GFP signal could be discerned over the cuticle autofluorescence (Figure 2A, top row, yellow arrowhead). In animals whose ODR-10::GFP levels were relatively low, the cuticle autofluorescence obscured the GFP fluorescence (Figure 2A, middle row, yellow arrowhead). No GFP fluorescence was seen in animals lacking the ODR-10::GFP transgene (Figure 2A, bottom row).

To differentiate between cuticle autofluorescence and GFP fluorescence, we characterized each using Fast-FLIM (i.e., average photon arrival time, Figure 2B). Regardless of expression level, the average photon arrival time of ODR-10::GFP was approximately 2.5 ns (Figure 2B, top and middle rows), and the average photon arrival time of cuticle autofluorescence was approximately 1.3 ns (Figure 2B, all rows). This suggested that FLIM could be used to separate these spectrally similar signals. However, Fast-FLIM has limited utility because it does not distinguish heterogeneous lifetimes within a single pixel. To more fully characterize cuticle and ODR-10::GFP fluorescence, we used Phasor-FLIM (Figure 2C). On phasor plots, the ODR-10::GFP signal is located near the unit semi-circle at approximately 2.5 ns (based upon the 80 mHz repetition rate of our laser), which is indicative of a single, well-defined lifetime (Figure 2C, yellow circle; Digman et al., 2008). In contrast, the cuticle signal is located in the interior of the unit semi-circle as a right shifted, tight cluster, which is indicative of shorter, heterogeneous

lifetimes (Figure 2C, magenta circle). These results suggest that cuticle autofluorescence arises from green fluorophores with complex decay profiles that can be spatially resolved in phasor space from the single component ODR-10::GFP. Indeed, when phasor masking is applied to these images, both bright and dim ODR-10::GFP signal can be faithfully "extracted" from cuticle autofluorescence in live animals (Figure 2D-F, top and middle rows). To demonstrate the biological usefulness of phasor masking, we used this process to characterize how the genetic mutation of the putative E2 ubiquitin ligase, *ubc-6,* affects ODR-10::GFP abundance. *ubc-6* is a highly conserved eukaryotic gene that participates in ER-associated degradation (Christianson & Carvalho, 2022; Weber et al., 2016), but no previous studies have implicated it in olfactory receptor maintenance. We found that a deletion in the *ubc-6* gene results in a 2.7-fold increase in the ciliary accumulation of ODR-10::GFP (average total photon counts for wildtype = 6075, *ubc-6* mutant = 16657, student's t-test p-value <0.001; Figure 2G-H).

Our results establish that Phasor-FLIM can separate problematic cuticle autofluorescence from GFP fluorescence in dim ciliated neurons located in the head of the animal. Next, we investigated whether spectral emission scanning and FLIM could be combined to differentiate between populations of gut autofluorescence in the anterior of the animal (Figure 3A), which is known to result from a heterogeneous collection of subcellular lysosome-related gut granules (Hermann et al., 2005; Morris et al., 2018). Similar to our lower resolution spectral analysis (Figure 1), the anterior gut produced heterogeneous emission spectra from individual granules that was most strongly stimulated with the 405 nm and 473 nm laser lines (Figure 3B and 3C). To more fully characterize the heterogeneity, we applied K means clustering to spectral profiles of individual granules produced by 405 nm excitation. Specifically, we used the summed mean emission intensity across all wavelengths (i.e., brightness) as one component and the intensity weighted center of the emission peak (i.e., center of mass) as the second component. The clustering analysis revealed four robust populations (Figure 3D and 3E, Supplemental Figure 3). The brightest population had a center of mass at approximately 525 nm (Figure 3D and 3E, magenta) and included both isolated granules and granules that overlap with a larger, dimmer population (Figure 3F and 3G, yellow). There were two additional relatively dim populations with centers of mass at approximately 495 nm and 510 nm (Figure 3D-G, cyan and grey, respectively). These results demonstrate that high spatial resolution emission scanning can be combined with unbiased clustering approaches to phenotype spectrally distinct granules.

Because GFP fluorescence could be separated from spectrally similar cuticle autofluorescence using FLIM (Figure 2), we were curious whether FLIM could also reveal different subpopulations of gut granules. To test this, we analyzed fluorescence lifetime in several anterior and posterior regions of the gut using a 473 nm excitation laser (Figure 4A). The photon count (i.e., intensity) images revealed granules with a range of intensities. These included both homogenous granules with uniform intensity and granules that appeared to have multiple compartments (Figure 4B and 4D, left column; Supplemental Figure 4). Intriguingly, some of these granules could be visually distinguished via Fast-FLIM (Figure 4B and 4D, middle column; Supplemental Figure 4). We analyzed phasor plots to further understand the nature of the different fluorescent lifetime populations. Phasor analysis revealed 3 distinct subpopulations of multi-component autofluorescence (i.e., located in the interior of the phasor plot) that originated from spatially distinct gut particles (Figure 4B, right column; magenta, *a*; yellow, *b*; and cyan, *c*). Generally, the magenta phasor population (Figure 4C, *a*) was composed of relatively large, low intensity granules that were sparsely distributed across the gut. In contrast, the yellow and cyan populations included both well-defined granules and diffuse regions of autofluorescence that lacked clear boundaries (Figure 4C, *b* and *c*). In addition, we also observed individual granules that could be separated into spatially distinct areas of the phasor plot (Figure 4D, right column). Specifically, within a mixed population, some – but not all – granules could be separated into more than one lifetime (compare Figure 4E, *a-c,* magenta, *a*; magenta and cyan, *b*; and cyan only, *c*). Collectively, these results demonstrate that spatially distinct gut granule autofluorescence can be more fully characterized in a label free manner through a combination of high resolution spectral and Phasor-FLIM analysis.

FLIM is advancing as a useful tool to overcome challenging microscopy problems (Datta et al., 2020) that include label-free analysis of autofluorescent cell structures and molecules (Blacker et al., 2014; Ouyang et al., 2021), biochemical characterization of the solvent surrounding known fluorophores (Llères et al., 2017), and distinguishing spectrally similar fluorophores (Scipioni et al., 2021). Here, we used FLIM to facilitate traditionally problematic quantification of dim GFP signal within sub-micron scale cell structures (i.e., sensory cilia) that are obscured by the green component of cuticle autofluorescence (Figure 2 and as seen in (Sepulveda et al., 2023; Wang et al., 2015)). Compared to prior techniques, our FLIM method has the major benefit of not requiring the re-engineering of strains with different fluorescent reporters (Heppert et al., 2016) or purchasing an extensive array of overlapping bandpass filters (Morris et al., 2018). Although FLIM setups themselves can be costly and technically complex, as commercial systems become more common it is expected that using FLIM to isolate and quantify GFP

signal will become more accessible. Moreover, because cuticle autofluorescence (Figure 2) and gut autofluorescence (Figure 4) exhibit complex decay profiles (i.e., they map to the interior of the phasor plot), the autofluorescence elimination approach described in this manuscript should be able to distinguish autofluorescence from any fluorescent protein that exhibits mono-exponential decay.

In addition, we have used FLIM to reveal sub-populations of autofluorescent lysosome-related organelles (gut granules) that can be separated based upon lifetime differences alone. This complements recent analytical approaches that combine Nile Red staining with two-photon FLIM to differentiate gut granules with distinct lipid populations (W.-W. Chen et al., 2023). We have also used excitation/emission scanning to identify spectrally distinct subpopulations of gut granules that are uniquely excited at 405 nm. In the future, it will be important to identify how these spectrally distinct gut granules relate to those that can be distinguished via FLIM alone. However, this will require a pulsed UV laser to simultaneously excite the spectrally distinct population and perform time-correlated single photon counting, which is not presently available on commercial FLIM instruments.

C. elegans gut granules are an established model for understanding nutrient trafficking and metabolism. While many studies have focused on the endocytic pathways that underlie gut granule maturation, it is becoming clear that age and nutritional states can affect the physical, biochemical, and visual properties of gut granules (A.J. Chen et al., 2018; W.-W. Chen et al., 2023; Hermann et al., 2005; Roh et al., 2012). For example, when animals are reared in excess zinc, gut granules form with a bilobed morphology (Mendoza et al., 2024; Roh et al., 2012). Because only one of the lobes consistently contains high concentrations of zinc, these granules are physiologically and spatially asymmetric (Mendoza et al., 2024). Our observation of some gut granules that contain fluorescence with more than one lifetime species is particularly reminiscent of these bilobed granules (Mendoza et al., 2024; Roh et al., 2012), though we did not rear animals on artificially high zinc concentrations.

The gut granules that we describe in this manuscript appear to represent spectrally defined categories, but they are not homogeneous with respect to representation and localization (Figures 3 and 4, Supplemental Figures 3 and 4). This heterogeneity could arise from several aspects of *C. elegans* biology. First, because our samples were intentionally unlabeled, we did not attempt to identify different classifications of organelles. That is, it is possible that some of

the granules that appear in our images represent lysosomes, endosomes, or other compartments derived from the endomembrane system. In addition, lysosome related organelles (LROs) undergo changes within developing and aging *C. elegans*. For example, protein markers for LROs can be detected during late embryonic and early larval stages (Hermann et al., 2005), but changes in lipid accumulation in LROs continue later, as the animals reach reproductive maturity and yolk proteins and lipids are transferred to maturing oocytes (Komura et al., 2021; Schroeder et al., 2007). Birefringence in LROs also increases as animals age (Komura et al., 2021). While we imaged animals after their final molt (from L4 larvae to adult animals), it is possible that our imaging captured granules that were in different stages of maturity. Finally, LROs are increasingly recognized as centers of metabolic regulation and metabolite storage. In particular, LROs can accumulate zinc (Roh et al., 2012), copper (Chun et al., 2017), and anthranilic acid glucosyl ester (downstream of kynurenine pathway, reviewed in (Coburn & Gems, 2013)). Importantly, even in animals experiencing a high metabolic input (for example, high levels of zinc), changes in gut granules labeling, size, and shape are heterogeneous (Roh et al., 2012). In our own analysis, we found some heterogeneity in spectral and FLIM profiles depending on where images were located (Supplemental Figure 3 and Supplemental Figure 4). Overall, our data may be capturing the existing heterogeneity in the gut granule populations. Future experiments in animals lacking LROs, for example *glo-1* mutants (Hermann et al., 2005; Rabbitts et al., 2008), could be used to parse the precise identity of the granules we have described. In addition, monitoring and/or intentionally modifying metabolic inputs could drive gut granules to more heterogeneous spectral profiles.

Our imaging data show that autofluorescence can be masked to remove signal that may interfere with fluorescence imaging. With respect to understanding the biology of endomembrane trafficking in the gut, this is important because gut granule autofluorescence complicates the imaging and analysis of particles as they mature (Rabbitts et al., 2008; Voss et al., 2020). Previously, researchers depended on specific filter sets and protocols to try to remove background autofluorescence (Teuscher & Ewald, 2018). Alternatively, lipophilic or metal-binding dyes have been effective at boosting the signal of organelles of interest (Mendoza et al., 2024; Sepulveda et al., 2023). Recently, gut granule stores of heme have been assessed in a dye-free assay using transient absorption microscopy, but this relies specifically on the chemical signature of heme (A. J. Chen et al., 2018). Our FLIM data suggest that biochemical differences within subpopulations, and even individual gut granules, could be differentiated without the need for labeling or knowledge of precise chemical differences. Collectively, our

results demonstrate that high spatial resolution spectral scanning combined with Phasor-FLIM is a useful tool to overcome challenging live imaging problems in *C. elegans* biology.

Methods:

***C. elegans* strains used in this study:** N2 (Bristol), *kyIs53* (P*odr-10::ODR-10::*GFP), *kyIs53*; *ubc-7* (*gk857464*), *kyIs53*; *ubc-6* (*gk3799 gk5313[loxP*]). *C. elegans* were maintained according to accepted protocols (Brenner, 1974; Meneely et al., 2019).

Preparing slides: Animals were grown at 21.5 ºC on nematode growth media (NGM) spotted with OP-50 *E. coli*. Animals were age synchronized by dissolving gravid animals and allowing the remaining eggs to hatch on NGM plates (Porta-de-la-Riva et al., 2012). Age synchronized young adult animals were paralyzed in an 8 μL droplet of 30 mg/mL 2,3-butanedione monoxime on a glass coverslip for 10 minutes. A 2% agarose pad was used to hold the fully immobilized animals for imaging.

Microscope description: All imaging was performed on a Leica Stellaris 8 equipped with an 80 mHz pulsed white light laser that is tunable in 1 nm increments from 440-790 nm, a 405 nm diode (non-pulsed) laser, and five HyD detectors with dispersion-based spectral scanning from 410-850 nm. The microscope is equipped with a 63X 1.4 NA oil objective, a 63X 1.2 NA water objective, a 40X 1.4 NA oil objective, 25X 0.95 NA water objective, 20X 0.75 NA dry objective, 10X 0.4 NA dry objective. The microscope is controlled by LasX software that includes the Falcon FLIM module (including phasor analysis), Lightning deconvolution, and TauSense. For all imaging experiments, the 405 diode and white light laser were both turned on 45 minutes before data was collected to allow them to warm up. All laser intensities reported in this manuscript are relative – laser power at the sample was not determined.

Spectral Scans of entire *C. elegans*: To capture emission profiles of the entire animal, the 20x/0.75 objective lens was used with a digital zoom of 4.44 to create a tile scan of the animal with a 256.19 nm pixel size. To capture emission profiles of gut granules, the 63X/1.4 oil objective lens was used with a digital zoom of 5.26 to create single images with a pixel size of 68.65 nm. The focal plane for the emission scanning was approximately midway through the animal. Four commonly used excitation wavelengths (405 nm, 473 nm, 561 nm, and 647 nm) were used to create emission profiles in 30 nm increments from 420-780 nm (405 nm

excitation), 480-780 nm (473 nm excitation), 570-780 nm (561 nm excitation), and 660-780 nm (647 nm excitation). The spectral scan information is stored in image stacks where each slice contains the intensity information for a 30 nm band of the emission profile (see Supplemental Figure 1B-D for an example of spectral image stack).

Colorized Spectral Images and Spectral Plots: To create spectral plots of the entire animal (Figure 1D) or of individual gut regions (Figure 3C) the average intensity per unit area was calculated for regions of interest and plotted against the center of the respective emission band. To colorize the spectral image data, the slice corresponding to each emission band was converted to an RGB color corresponding to the average wavelength for that emission band (e.g., 435 nm (blue) for the 420-450 nm band and 645 nm (red) for the 630-660 nm band). These RGB images were then summed to produce a fully colorized image. For example, if a region of interest had strong emission in the blue, green, and red bands, the summed colorized image would appear white, but if there was strong emission in green and red bands, the summed colorized image would appear yellow. The same steps were followed for "brightened colorized" images, except the contrast was adjusted to saturate <= 0.125% of pixels before making the figure. To characterize gut granule emission, the R program Kmeans++ was used to cluster individual gut granules based upon the summed mean intensity (i.e., brightness) and the center of mass (i.e., color) of their spectral profiles (Figure 3D-G and Supplemental Figure 3). The gut granules were manually outlined in FIJI prior to Kmeans++ clustering.

General Procedure for Separating Cuticle Autofluorescence from GFP Fluorescence: Images were acquired as Z-stacks with a 1 μm step size using a 63x/1.40 oil objective, a zoom of 4, and a resolution of 512x512 pixels, which leads to a 90 nm pixel size. The scan speed was set to 600 Hz with four-line repetitions and the 488 nm laser set to 100% power. The acquisition was conducted using LasX FALCON/FLIM, which sets the emission detector to single photon counting mode and synchronizes the electronics to operate as a time-correlated single photon counter. Photon Count images represent the total number of photons collected at each pixel (i.e., intensity). Fast-FLIM images represent the average photon arrival time at each pixel. Phasor analysis was performed with the following settings: Pixel Binning: 1, Harmonic: 1, Threshold: 15 photons, Median Filter Radius: 11 pixels. After identifying the phasor space that contained the GFP signal and the autofluorescence signal, a circular phasor mask was created to encapsulate the appropriate area. After a region of the phasor plot was selected in LasX, the corresponding image pixels were exported as a mask. To mask GFP, a 50-pixel circle centered

at 2.561 ns was used. To mask cuticle autofluorescence, a 30-pixel circle centered at 1.017 ns was used. The mask images were imported into ImageJ where all pixels outside of the mask were set to 0.

Quantification of ODR-10::GFP accumulation in AWA cilia: Images of wild-type and *ubc-6* mutant animals were obtained with the following settings: Objective: 63x/1.40 oil, resolution: 512x512, zoom: 4, pixel size: 90 nm, step size: 1 μm, scan speed: 600 Hz, line repetitions: 4, laser: 488nm excitation with 50% intensity. FLIM characterization was performed with the following settings: Pixel Binning: 1, Harmonic: 1, Threshold: 7 photons, Median Filter Radius: 19. GFP signal was extracted as described above. The resulting GFP images were processed using a FIJI macro found here: https://github.com/heinohv/Dahlberg-Lab/blob/main/photon_measure.ijm.

FLIM analysis of Gut Granules: The images were captured with the following settings: Objective: 63x/1.40 oil, resolution: 512x512, zoom: 5.26, pixel size: 69 nm, scan speed: 600 Hz, line repetitions: 8, laser: 473 nm excitation with 10% intensity. FLIM characterization and export was performing with the following settings: Pixel binning: 2, Hamonic: 1, Threshold 20-100 photons, Median Filter Radius: 11. To characterize different granules based on fluorescent lifetime, phasor plots were manually scanned to identify gut granules, or parts of gut granules, whose autofluorescence could be mapped back to discrete regions of phasor space.

Acknowledgements:

ubc-6 and *ubc-7* mutant strains were originally a kind gift from the Moerman Laboratory, University of British Columbia and are now publicly available at the CGC.

Competing Interests:

No competing interests declared.

Funding:

Some *C. elegans* strains were provided by the CGC, which is funded by National Institute of Health (NIH) Office of Research Infrastructure Programs (P40 OD010440). The Leica Stellaris 8 FALCON/FLIM microscope was purchased and maintained with support from a National Science Foundation (NSF) Major Research Instrumentation grant (NSF DBI 2019228). Additional microscopy support was provided by the WWU Scientific Technical Services Optical

Microscopy Core Facility. FLIM research in the Galati Lab is supported by WWU startup funds and an NSF CAREER grant (NSF BIO 2146516).

Data and resource availability:

All relevant data and resources can be found within the article and its supplementary information.

Figure Legends:

Figure 1: *C. elegans* autofluorescence is most prominent at shorter wavelengths. A) An image of a 3-day old *C. elegans* acquired using differential interference contrast (DIC). B) Colorized spectral images of a single plane in the same animal in (A) showing autofluorescence emission after excitation with the following laser lines: 405 nm (emission 420-780 nm), 473 nm (emission 480-780 nm), 561 nm (emission 570-780 nm), and 647 nm (emission 660-780 nm). Relative laser power is reported as a percentage. Regions of gut (asterisk) and cuticle (box and arrowhead) autofluorescence are distinguished in the 473 nm excitation image. C) A mock spectral profile of *C. elegans.* The excitation wavelength is represented by a vertical bar (purple). The emission was collected in 30 nm bins and plotted as mean arbitrary fluorescence units (AFU) per μm^2. D) The spectral profiles for each colorized spectral image in panel (B). See Materials and Methods and Supplemental Figure 1 for detailed explanation of how images were colorized and converted to spectral profiles. Similar spectral profiles were generated for five additional independent animals during two imaging sessions (presented in Supplemental Figure 2).

Figure 2: Phasor-FLIM masking to isolate GFP fluorescence from autofluorescence. Column A) Maximum intensity projections of *C. elegans* head showing high, low, or no GFP fluorescence in the AWA neuron excited with a 473 nm laser line. The cuticle and neuron are indicated with magenta and yellow arrows, respectively. Images are scaled to avoid saturation of the GFP signal. Genotypes imaged were *ubc-7* (*gk857464*); *kyIs53* (top), *kyIs53* (middle), N2 (bottom). Column B) Fast-FLIM images displayed with a time-coded lookup table (LUT) showing longer lifetime GFP fluorescence (green/yellow) and shorter lifetime autofluorescence (cyan). Column C) Phasor plots that correspond to the Fast-FLIM images in column (B). The yellow circle encapsulates the phasor space corresponding to GFP fluorescence. The magenta circle encapsulates the phasor space corresponding to cuticle autofluorescence. The horizontal axis of the phasor plot represents the *g* component, while the vertical axis represents the *s* component. The single exponential lifetime for pixels that fall on the universal semi-circle are between 0 and 12 ns, which is based upon the laser repetition rate of 80 mHz. Column D) False colored images showing the GFP (yellow) and cuticle autofluorescence (magenta) regions of the phasor plots shown in column C. Columns E and F) Maximum intensity projections of the GFP pixels (column E) and cuticle autofluorescence pixels (column F) as defined in column D. These results were generated from three independent animals imaged in a single imaging session. G) Representative images of Phasor-FLIM masking applied to kyIs53 worms in a wild-type and *ubc-6* mutant background. H) GFP signal quantified and compared between the wild-

type and *ubc-6* mutant background. 36 wild-type animals were imaged over six imaging sessions; 15 *ubc*-6 mutant animals were imaged over three imaging sessions. Normality of each group was checked using a Shapiro-Wilk test (Wild-type: p=0.18, *ubc-6*: p=0.61). Groups were then compared using a two-tailed Student's t-test, which indicated a significant difference ($p < 0.001$).

Figure 3: Autofluorescent granules have spectrally distinct populations and regions. A) A schematic representation of a 3-day old *C. elegans* and a region of the upper intestine captured at 63X magnification (inset) using DIC. B) Images of a single plane in the intestine region (A, inset) showing autofluorescence emission after excitation with the following laser lines: 405 nm (emission 420-780 nm), 473 nm (emission 480-780 nm), 561 nm (emission 570-780 nm), and 647 nm (emission 660-780 nm). The left column shows total photon count as a greyscale image with the excitation wavelength and relative laser power is reported as a percentage. The middle column shows colorized spectral images. The right column shows brightened colorized spectral images. C) The spectral profiles for each colorized spectral image in panel B. D) Colorized spectral images of granules stimulated with the 405 nm laser line. Outlines indicate regions of interest that were quantified across the entire emission spectrum. E) Left, the average emission of 187 granules across 6 images from 6 different animals outlined within the field of view, as shown in D (line color refers to the outline and the shading around the central line shows standard deviation from the average). Right, Kmeans++ clustering identifies four clusters of granules based on their spectral center of mass and summed mean intensity. F) Colorized spectral images of granules from panels (A) and (B) that were stimulated with the 405 nm laser line. G) Kmeans++ analysis showing that granules and sub-regions of granules are distributed across three of the four clusters identified in (E).

Figure 4: Sub-populations of gut granules have distinct multi-exponential lifetimes and regions with distinct fluorescent lifetimes. A) A schematic representation of a 3-day old *C. elegans.* Four gut regions were imaged with high spatial resolution FLIM (white boxes, regions 1-4). B) Photon count images (left column), time-coded Fast-FLIM images (middle column), and photon count images with phasor overlay (phasor mask, right column) of a single plane in regions 1 and 2. The color scale for lifetime value is located above the column of Fast-FLIM images. C) Zoomed images of granules with distinct multi-exponential lifetimes identified at the regions indicated in the phasor plot below (*a*, magenta; *b*, yellow; *c*, cyan). D) Photon count images (left column), time-coded Fast-FLIM images (middle column), and photon count images with phasor overlay (phasor mask, right column) of a single plane in regions 3 and 4. The color

scale for lifetime value is located above the column of Fast-FLIM images. E) Zoomed images of granules composed of a single lifetime (*a,* magenta only and *c,* cyan only) and two examples of granules composed of two lifetimes (*b*, magenta and cyan). These results are representative of similar results that were replicated in four different animals across four different imaging sessions on four separate days.

Supplemental Figure 1. Generation of colorized images based on spectral scanning. A) Image of the animal shown in Figure 1. The white box indicates the portion of the animal used for this colorization example. B) XY Lambda (emission) stacks were split into 12 individual emission bins. C) Each emission bin was colorized based on the center of the emission bin. For example, for the 420-450 nm emission bin, the blue color LUT corresponds to different intensities of 435 nm light. D) Images from B are displayed with a narrow intensity range to make the dim signal more apparent. E) A generic spectral profile plot showing how each emission bin image corresponds to an emission bin average in the spectral profile plot.

Supplemental Figure 2. Variable emission is stimulated by the 561 nm laser line. 3-day old *C. elegans* acquired using differential interference contrast (DIC) and the same spectral scanning approach described in Figure 1. A-E) show consistent strong emission stimulated by the 405 nm and 473 nm laser lines. A-C) show weak but observable emission stimulated by the 561 nm laser line. D and E) show barely detectable emission stimulated by the 561 nm laser line. These results were generated from five independent animals imaged across two separate imaging sessions on two separate days.

Supplemental Figure 3. Individual spectral profiles for spectrally distinct gut granules separated via Kmeans++ clustering. The individual spectral profiles for all 187 gut granules acquired from 6 separate animals that were analyzed in this study. The color coding of the spectral profiles was determined via Kmeans++ clustering. The average and standard deviation for each class of spectral profile is shown in Figure 3E.

Supplemental Figure 4. Additional examples of autofluorescence with spatial heterogeneity in fluorescence lifetime throughout the gut of *C. elegans*. A) A schematic representation of a 3-day old *C. elegans.* As in Figure 4, single planes in four gut regions were imaged with high spatial resolution FLIM (white boxes, regions 1-4). B) Photon count images (left column), time-coded Fast-FLIM images (middle column), and photon count images with phasor overlay (phasor mask, right column) of regions 1 and 2. The color scale for lifetime value is located above the column of Fast-FLIM images. C) Zoomed images of granules with distinct

multi-exponential lifetimes identified at the regions indicated in the phasor plot below (*a*, magenta; *b*, yellow; *c*, cyan). D) Photon count images (left column), time-coded Fast-FLIM images (middle column), and photon count images with phasor overlay (phasor mask, right column) of regions 3 and 4. The color scale for lifetime value is located above the column of Fast-FLIM images. E) Zoomed images of granules composed of a single lifetime (*a*, magenta only and *c*, cyan only) and two examples of granules composed of two lifetimes (*b*, magenta and cyan). These results are representative of similar results that were replicated in four different animals across four different imaging sessions on four separate days.

Bibliography

Bao, Z., Murray, J. I., Boyle, T., Ooi, S. L., Sandel, M. J., & Waterston, R. H. (2006). Automated cell lineage tracing in Caenorhabditis elegans. *Proceedings of the National Academy of Sciences*, *103*(8), 2707–2712. https://doi.org/10.1073/pnas.0511111103

Bhattacharjee, A., Datta, R., Gratton, E., & Hochbaum, A. I. (2017). Metabolic fingerprinting of bacteria by fluorescence lifetime imaging microscopy. *Scientific Reports*, *7*(1), 3743. https://doi.org/10.1038/s41598-017-04032-w

Blacker, T. S., Mann, Z. F., Gale, J. E., Ziegler, M., Bain, A. J., Szabadkai, G., & Duchen, M. R. (2014). Separating NADH and NADPH fluorescence in live cells and tissues using FLIM. *Nature Communications*, *5*(1), 1–9. https://doi.org/10.1038/ncomms4936

Brenner, S. (1974). THE GENETICS OF *CAENORHABDITIS ELEGANS*. *Genetics*, *77*(1), 71–94. https://doi.org/10.1093/genetics/77.1.71

Chalfie, M., Tu, Y., Euskirchen, G., Ward, W. W., & Prasher, D. C. (1994a). Green Fluorescent Protein as a Marker for Gene Expression. *Science*, *263*(5148), 802–805. https://doi.org/10.1126/science.8303295

Chalfie, M., Tu, Y., Euskirchen, G., Ward, W. W., & Prasher, D. C. (1994b). Green fluorescent protein as a marker for gene expression. *Science (New York, N.Y.)*, *263*(5148), Article 5148.

Chen, A. J., Yuan, X., Li, J., Dong, P., Hamza, I., & Cheng, J.-X. (2018). Label-Free Imaging of Heme Dynamics in Living Organisms by Transient Absorption Microscopy. *Analytical Chemistry*, *90*(5), 3395–3401. https://doi.org/10.1021/acs.analchem.7b05046

Chen, W.-W., Tang, W., Hamerton, E. K., Kuo, P. X., Lemieux, G. A., Ashrafi, K., & Cicerone, M. T. (2023). Identifying lipid particle sub-types in live Caenorhabditis elegans with two-photon fluorescence lifetime imaging. *Frontiers in Chemistry*, *11*. https://www.frontiersin.org/articles/10.3389/fchem.2023.1161775

Christianson, J. C., & Carvalho, P. (2022). Order through destruction: How ER-associated protein degradation contributes to organelle homeostasis. *The EMBO Journal*, *41*(6), e109845. https://doi.org/10.15252/embj.2021109845

Chun, H., Sharma, A. K., Lee, J., Chan, J., Jia, S., & Kim, B.-E. (2017). The Intestinal Copper Exporter CUA-1 Is Required for Systemic Copper Homeostasis in *Caenorhabditis elegans**♦. *Journal of Biological Chemistry*, *292*(1), 1–14. https://doi.org/10.1074/jbc.M116.760876

Chung, S. H., Sun, L., & Gabel, C. V. (2013). In vivo Neuronal Calcium Imaging in C. elegans. *JoVE (Journal of Visualized Experiments)*, *74*, e50357. https://doi.org/10.3791/50357

Coburn, C., & Gems, D. (2013). The mysterious case of the C. elegans gut granule: Death fluorescence, anthranilic acid and the kynurenine pathway. *Frontiers in Genetics*, *4*, 151. https://doi.org/10.3389/fgene.2013.00151

Corsi, A. K., Wightman, B., & Chalfie, M. (2015). A Transparent Window into Biology: A Primer on Caenorhabditis elegans. *Genetics*, *200*(2), 387–407. https://doi.org/10.1534/genetics.115.176099

Datta, R., Heaster, T. M., Sharick, J. T., Gillette, A. A., & Skala, M. C. (2020). Fluorescence lifetime imaging microscopy: Fundamentals and advances in instrumentation, analysis, and applications. *Journal of Biomedical Optics*, *25*(7), 071203. https://doi.org/10.1117/1.JBO.25.7.071203

Digman, M. A., Caiolfa, V. R., Zamai, M., & Gratton, E. (2008). The Phasor Approach to Fluorescence Lifetime Imaging Analysis. *Biophysical Journal*, *94*(2), L14–L16. https://doi.org/10.1529/biophysj.107.120154

Eichel, K., Uenaka, T., Belapurkar, V., Lu, R., Cheng, S., Pak, J. S., Taylor, C. A., Südhof, T. C., Malenka, R., Wernig, M., Özkan, E., Perrais, D., & Shen, K. (2022). Endocytosis in the axon initial segment maintains neuronal polarity. *Nature*, *609*(7925), Article 7925. https://doi.org/10.1038/s41586-022-05074-5

El Mouridi, S., Alkhaldi, F., & Frøkjær-Jensen, C. (2022). Modular safe-harbor transgene insertion for targeted single-copy and extrachromosomal array integration in Caenorhabditis elegans. *G3 Genes|Genomes|Genetics*, *12*(9), jkac184. https://doi.org/10.1093/g3journal/jkac184

Gallrein, C., Iburg, M., Michelberger, T., Koçak, A., Puchkov, D., Liu, F., Ayala Mariscal, S. M., Nayak, T., Kaminski Schierle, G. S., & Kirstein, J. (2021). Novel amyloid-beta pathology *C. elegans* model reveals distinct neurons as seeds of pathogenicity. *Progress in Neurobiology*, *198*, 101907. https://doi.org/10.1016/j.pneurobio.2020.101907

Gonzalez Pisfil, M., Nadelson, I., Bergner, B., Rottmeier, S., Thomae, A. W., & Dietzel, S. (2022). Stimulated emission depletion microscopy with a single depletion laser using five fluorochromes and fluorescence lifetime phasor separation. *Scientific Reports*, *12*(1), 14027. https://doi.org/10.1038/s41598-022-17825-5

Hendler-Neumark, A., Wulf, V., & Bisker, G. (2021). In vivo imaging of fluorescent single-walled carbon nanotubes within C. elegans nematodes in the near-infrared window. *Materials Today Bio*, *12*, 100175. https://doi.org/10.1016/j.mtbio.2021.100175

Heppert, J. K., Dickinson, D. J., Pani, A. M., Higgins, C. D., Steward, A., Ahringer, J., Kuhn, J. R., & Goldstein, B. (2016). Comparative assessment of fluorescent proteins for in vivo imaging in an animal model system. *Molecular Biology of the Cell*, *27*(22), 3385–3394. https://doi.org/10.1091/mbc.E16-01-0063

Hermann, G. J., Schroeder, L. K., Hieb, C. A., Kershner, A. M., Rabbitts, B. M., Fonarev, P., Grant, B. D., & Priess, J. R. (2005a). Genetic Analysis of Lysosomal Trafficking in Caenorhabditis elegans. *Molecular Biology of the Cell*, *16*(7), 3273–3288. https://doi.org/10.1091/mbc.E05-01-0060

Hermann, G. J., Schroeder, L. K., Hieb, C. A., Kershner, A. M., Rabbitts, B. M., Fonarev, P., Grant, B. D., & Priess, J. R. (2005b). Genetic analysis of lysosomal trafficking in Caenorhabditis elegans. *Molecular Biology of the Cell*, *16*(7), 3273–3288. https://doi.org/10.1091/mbc.e05-01-0060

Jones, K. T., & Ashrafi, K. (2009). Caenorhabditis elegans as an emerging model for studying the basic biology of obesity. *Disease Models & Mechanisms*, *2*(5–6), 224–229. https://doi.org/10.1242/dmm.001933

Komura, T., Yamanaka, M., Nishimura, K., Hara, K., & Nishikawa, Y. (2021a). Autofluorescence as a noninvasive biomarker of senescence and advanced glycation end products in Caenorhabditis elegans. *Npj Aging and Mechanisms of Disease*, *7*(1), Article 1. https://doi.org/10.1038/s41514-021-00061-y

Komura, T., Yamanaka, M., Nishimura, K., Hara, K., & Nishikawa, Y. (2021b). Autofluorescence as a noninvasive biomarker of senescence and advanced glycation end products in Caenorhabditis elegans. *Npj Aging and Mechanisms of Disease*, *7*(1), 1–11. https://doi.org/10.1038/s41514-021-00061-y

Laine, R. F., Sinnige, T., Ma, K. Y., Haack, A. J., Poudel, C., Gaida, P., Curry, N., Perni, M., Nollen, E. A. A., Dobson, C. M., Vendruscolo, M., Kaminski Schierle, G. S., & Kaminski, C. F. (2019). Fast Fluorescence Lifetime Imaging Reveals the Aggregation Processes of α-Synuclein and

Polyglutamine in Aging Caenorhabditis elegans. *ACS Chemical Biology*, *14*(7), 1628–1636. https://doi.org/10.1021/acschembio.9b00354

Llères, D., Bailly, A. P., Perrin, A., Norman, D. G., Xirodimas, D. P., & Feil, R. (2017). Quantitative FLIM-FRET Microscopy to Monitor Nanoscale Chromatin Compaction In Vivo Reveals Structural Roles of Condensin Complexes. *Cell Reports*, *18*(7), 1791–1803. https://doi.org/10.1016/j.celrep.2017.01.043

Lou, J., Scipioni, L., Wright, B. K., Bartolec, T. K., Zhang, J., Masamsetti, V. P., Gaus, K., Gratton, E., Cesare, A. J., & Hinde, E. (2019). Phasor histone FLIM-FRET microscopy quantifies spatiotemporal rearrangement of chromatin architecture during the DNA damage response. *Proceedings of the National Academy of Sciences*, *116*(15), 7323–7332. https://doi.org/10.1073/pnas.1814965116

Ma, N., Digman, M. A., Malacrida, L., & Gratton, E. (2016). Measurements of absolute concentrations of NADH in cells using the phasor FLIM method. *Biomedical Optics Express*, *7*(7), 2441–2452. https://doi.org/10.1364/BOE.7.002441

Malacrida, L., Ranjit, S., Jameson, D. M., & Gratton, E. (2021). The Phasor Plot: A Universal Circle to Advance Fluorescence Lifetime Analysis and Interpretation. *Annual Review of Biophysics*, *50*(1), 575–593. https://doi.org/10.1146/annurev-biophys-062920-063631

Mendoza, A. D., Dietrich, N., Tan, C.-H., Herrera, D., Kasiah, J., Payne, Z., Cubillas, C., Schneider, D. L., & Kornfeld, K. (2024). Lysosome-related organelles contain an expansion compartment that mediates delivery of zinc transporters to promote homeostasis. *Proceedings of the National Academy of Sciences*, *121*(7), e2307143121. https://doi.org/10.1073/pnas.2307143121

Meneely, P. M., Dahlberg, C. L., & Rose, J. K. (2019). Working with Worms: *Caenorhabditis elegans* as a Model Organism. *Current Protocols Essential Laboratory Techniques*, *19*(1), e35. https://doi.org/10.1002/cpet.35

Monici, M. (2005). Cell and tissue autofluorescence research and diagnostic applications. *Biotechnology Annual Review*, *11*, 227–256. https://doi.org/10.1016/S1387-2656(05)11007-2

Morris, C., Foster, O. K., Handa, S., Peloza, K., Voss, L., Somhegyi, H., Jian, Y., Vo, M. V., Harp, M., Rambo, F. M., Yang, C., & Hermann, G. J. (2018). Function and regulation of the Caenorhabditis elegans Rab32 family member GLO-1 in lysosome-related organelle biogenesis. *PLOS Genetics*, *14*(11), e1007772. https://doi.org/10.1371/journal.pgen.1007772

Ouyang, Y., Liu, Y., Wang, Z. M., Liu, Z., & Wu, M. (2021). FLIM as a Promising Tool for Cancer Diagnosis and Treatment Monitoring. *Nano-Micro Letters*, *13*(1), 133. https://doi.org/10.1007/s40820-021-00653-z

Pincus, Z., Mazer, T. C., & Slack, F. J. (2016). Autofluorescence as a measure of senescence in C. elegans: Look to red, not blue or green. *Aging (Albany NY)*, *8*(5), 889–898. https://doi.org/10.18632/aging.100936

Porta-de-la-Riva, M., Fontrodona, L., Villanueva, A., & Cerón, J. (2012). Basic Caenorhabditis elegans Methods: Synchronization and Observation. *Journal of Visualized Experiments*, *64*, 4019. https://doi.org/10.3791/4019

Rabbitts, B. M., Ciotti, M. K., Miller, N. E., Kramer, M., Lawrenson, A. L., Levitte, S., Kremer, S., Kwan, E., Weis, A. M., & Hermann, G. J. (2008a). *Glo-3* , a Novel *Caenorhabditis elegans* Gene, Is Required for Lysosome-Related Organelle Biogenesis. *Genetics*, *180*(2), 857–871. https://doi.org/10.1534/genetics.108.093534

Rabbitts, B. M., Ciotti, M. K., Miller, N. E., Kramer, M., Lawrenson, A. L., Levitte, S., Kremer, S., Kwan, E., Weis, A. M., & Hermann, G. J. (2008b). Glo-3, a novel Caenorhabditis elegans gene, is required for lysosome-related organelle biogenesis. *Genetics*, *180*(2), 857–871. https://doi.org/10.1534/genetics.108.093534

Rashtchian, S., Youssef, K., Rezai, P., & Tabatabaei, N. (2021). High-speed label-free confocal microscopy of Caenorhabditis elegans with near infrared spectrally encoded confocal microscopy. *Biomedical Optics Express*, *12*(6), 3607–3618. https://doi.org/10.1364/BOE.427685

Rodrigues, N. T. L., Bland, T., Borrego-Pinto, J., Ng, K., Hirani, N., Gu, Y., Foo, S., & Goehring, N. W. (2022). SAIBR: A simple, platform-independent method for spectral autofluorescence correction. *Development*, *149*(14), dev200545. https://doi.org/10.1242/dev.200545

Roh, H. C., Collier, S., Guthrie, J., Robertson, J. D., & Kornfeld, K. (2012a). Lysosome-Related Organelles in Intestinal Cells Are a Zinc Storage Site in C. elegans. *Cell Metabolism*, *15*(1), 88–99. https://doi.org/10.1016/j.cmet.2011.12.003

Roh, H. C., Collier, S., Guthrie, J., Robertson, J. D., & Kornfeld, K. (2012b). Lysosome-related organelles in intestinal cells are a zinc storage site in C. elegans. *Cell Metabolism*, *15*(1), 88–99. https://doi.org/10.1016/j.cmet.2011.12.003

Ryan, D. A., Miller, R. M., Lee, K., Neal, S. J., Fagan, K. A., Sengupta, P., & Portman, D. S. (2014). Sex, age, and hunger regulate behavioral prioritization through dynamic modulation of chemoreceptor expression. *Current Biology: CB*, *24*(21), 2509–2517. https://doi.org/10.1016/j.cub.2014.09.032

635 Schroeder, L. K., Kremer, S., Kramer, M. J., Currie, E., Kwan, E., Watts, J. L., Lawrenson, A. L., & Hermann,
636 G. J. (2007). Function of the Caenorhabditis elegans ABC Transporter PGP-2 in the Biogenesis of
637 a Lysosome-related Fat Storage Organelle. *Molecular Biology of the Cell*, *18*(3), 995–1008.
638 https://doi.org/10.1091/mbc.e06-08-0685
639 Scipioni, L., Rossetta, A., Tedeschi, G., & Gratton, E. (2021). Phasor S-FLIM: A new paradigm for fast and
640 robust spectral fluorescence lifetime imaging. *Nature Methods*, *18*(5), 542–550.
641 https://doi.org/10.1038/s41592-021-01108-4
642 Sengupta, P., Chou, J. H., & Bargmann, C. I. (1996). Odr-10 encodes a seven transmembrane domain
643 olfactory receptor required for responses to the odorant diacetyl. *Cell*, *84*(6), 899–909.
644 http://www.ncbi.nlm.nih.gov/pubmed/8601313
645 Sepulveda, N. B., Chen, D., & Petrella, L. N. (2023). Moderate heat stress-induced sterility is due to
646 motility defects and reduced mating drive in Caenorhabditis elegans males. *Journal of*
647 *Experimental Biology*, *226*(20), jeb245546. https://doi.org/10.1242/jeb.245546
648 Szmacinski, H., Toshchakov, V., & Lakowicz, J. R. (2014). Application of phasor plot and autofluorescence
649 correction for study of heterogeneous cell population. *Journal of Biomedical Optics*, *19*(4),
650 046017. https://doi.org/10.1117/1.JBO.19.4.046017
651 Teuscher, A. C., & Ewald, C. Y. (2018). Overcoming Autofluorescence to Assess GFP Expression During
652 Normal Physiology and Aging in Caenorhabditis elegans. *Bio-Protocol*, *8*(14), e2940.
653 https://doi.org/10.21769/BioProtoc.2940
654 Teuscher, A., & Ewald, C. (2018). Overcoming Autofluorescence to Assess GFP Expression During Normal
655 Physiology and Aging in Caenorhabditis elegans. *BIO-PROTOCOL*, *8*(14).
656 https://doi.org/10.21769/BioProtoc.2940
657 Thomas, B. J., Wight, I. E., Chou, W. Y. Y., Moreno, M., Dawson, Z., Homayouni, A., Huang, H., Kim, H.,
658 Jia, H., Buland, J. R., Wambach, J. A., Cole, F. S., Pak, S. C., Silverman, G. A., & Luke, C. J. (2019).
659 CemOrange2 fusions facilitate multifluorophore subcellular imaging in C. elegans. *PLOS ONE*,
660 *14*(3), e0214257. https://doi.org/10.1371/journal.pone.0214257
661 Tian, L., Hires, S. A., Mao, T., Huber, D., Chiappe, M. E., Chalasani, S. H., Petreanu, L., Akerboom, J.,
662 McKinney, S. A., Schreiter, E. R., Bargmann, C. I., Jayaraman, V., Svoboda, K., & Looger, L. L.
663 (2009). Imaging neural activity in worms, flies and mice with improved GCaMP calcium
664 indicators. *Nature Methods*, *6*(12), 875–881. https://doi.org/10.1038/nmeth.1398
665 Voss, L., Foster, O. K., Harper, L., Morris, C., Lavoy, S., Brandt, J. N., Peloza, K., Handa, S., Maxfield, A.,
666 Harp, M., King, B., Eichten, V., Rambo, F. M., & Hermann, G. J. (2020). An ABCG Transporter

Functions in Rab Localization and Lysosome-Related Organelle Biogenesis in *Caenorhabditis elegans*. *Genetics*, *214*(2), 419–445. https://doi.org/10.1534/genetics.119.302900

Wang, J., Kaletsky, R., Silva, M., Williams, A., Haas, L. A., Androwski, R. J., Landis, J. N., Patrick, C., Rashid, A., Santiago-Martinez, D., Gravato-Nobre, M., Hodgkin, J., Hall, D. H., Murphy, C. T., & Barr, M. M. (2015). Cell-Specific Transcriptional Profiling of Ciliated Sensory Neurons Reveals Regulators of Behavior and Extracellular Vesicle Biogenesis. *Current Biology*, *25*(24), 3232–3238. https://doi.org/10.1016/j.cub.2015.10.057

Weber, A., Cohen, I., Popp, O., Dittmar, G., Reiss, Y., Sommer, T., Ravid, T., & Jarosch, E. (2016). Sequential Poly-ubiquitylation by Specialized Conjugating Enzymes Expands the Versatility of a Quality Control Ubiquitin Ligase. *Molecular Cell*, *63*(5), 827–839. https://doi.org/10.1016/j.molcel.2016.07.020

Yemini, E., Lin, A., Nejatbakhsh, A., Varol, E., Sun, R., Mena, G. E., Samuel, A. D. T., Paninski, L., Venkatachalam, V., & Hobert, O. (2021). NeuroPAL: A Multicolor Atlas for Whole-Brain Neuronal Identification in C. elegans. *Cell*, *184*(1), 272-288.e11. https://doi.org/10.1016/j.cell.2020.12.012

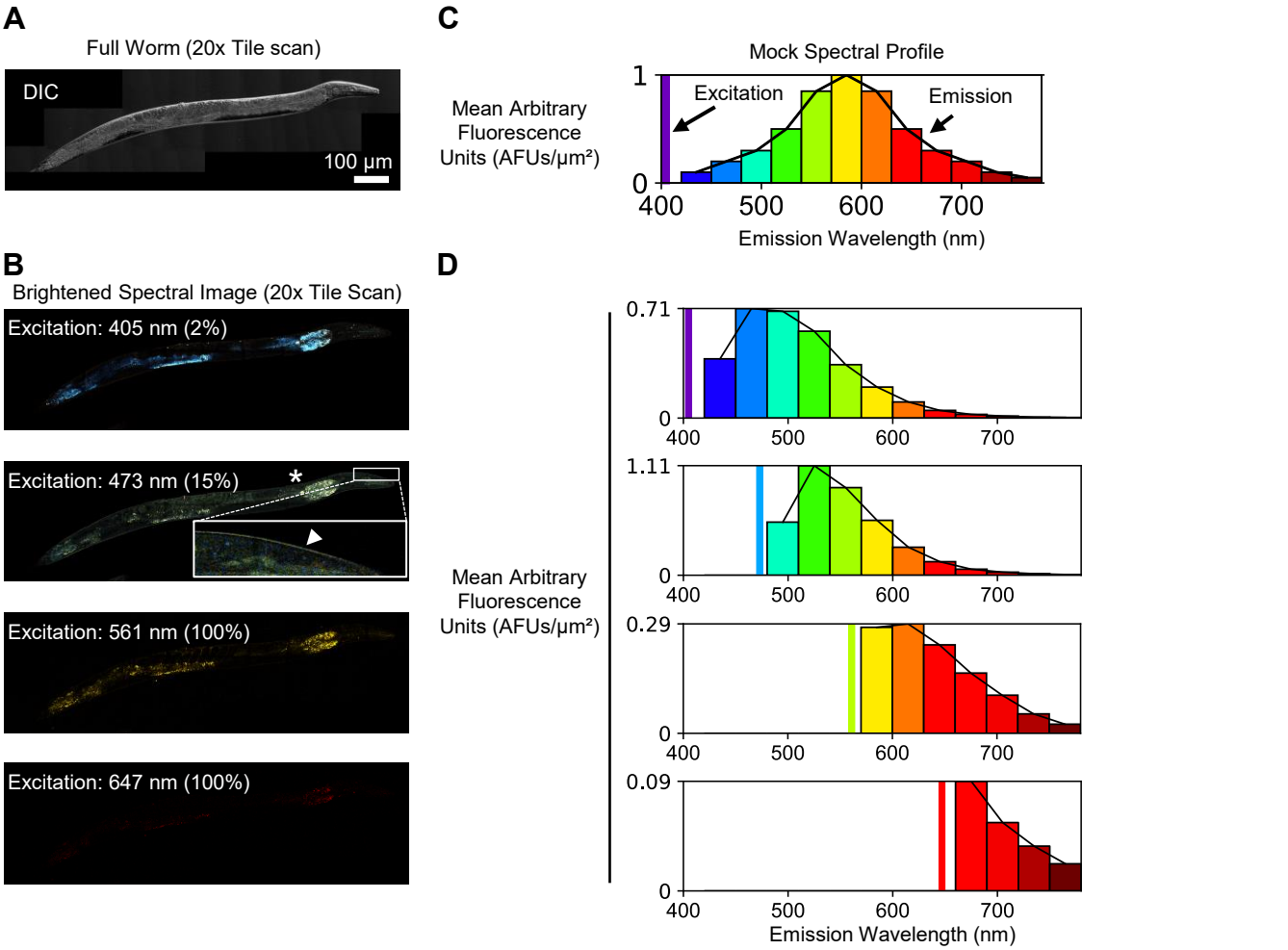
A
Full Worm (20x Tile scan)
DIC
100 µm
B
Brightened Spectral Image (20x Tile Scan)
Excitation: 405 nm (2%)
Excitation: 473 nm (15%)
*
Excitation: 561 nm (100%)
Excitation: 647 nm (100%)
C
Mock Spectral Profile
Mean Arbitrary Fluorescence Units (AFUs/µm²)
1
0
Excitation
Emission
400
500
600
700
Emission Wavelength (nm)
D
Mean Arbitrary Fluorescence Units (AFUs/µm²)
0.71
1.11
0.29
0.09
0
400
500
600
700
Emission Wavelength (nm)

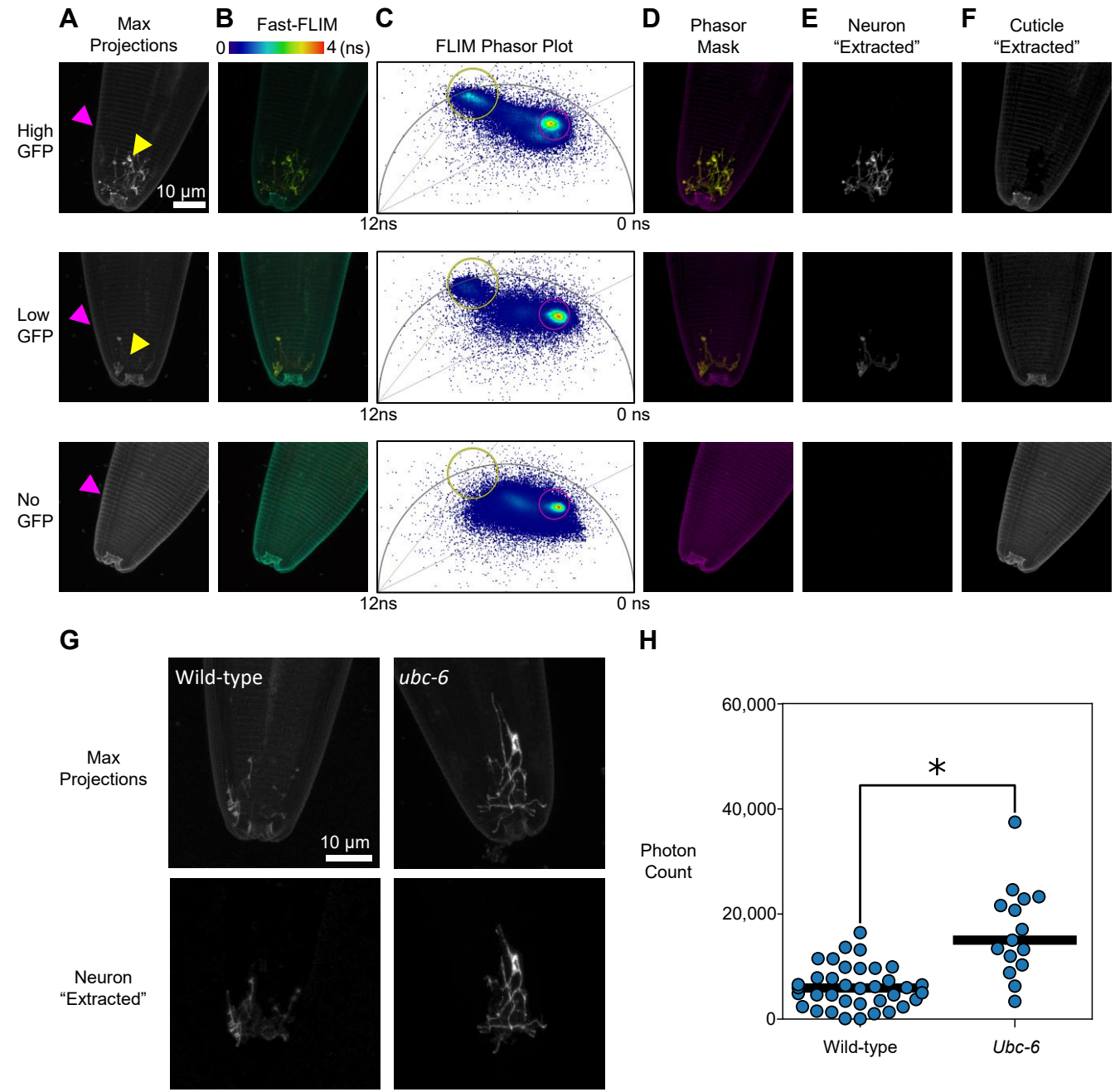
A
Max Projections
B
Fast-FLIM
0
4 (ns)
C
FLIM Phasor Plot
D
Phasor Mask
E
Neuron "Extracted"
F
Cuticle "Extracted"
High GFP
Low GFP
No GFP
10 µm
12ns
0 ns
12ns
0 ns
12ns
0 ns
G
Max Projections
Neuron "Extracted"
Wild-type
ubc-6
10 µm
H
Photon Count
60,000
40,000
20,000
0
*
Wild-type
Ubc-6

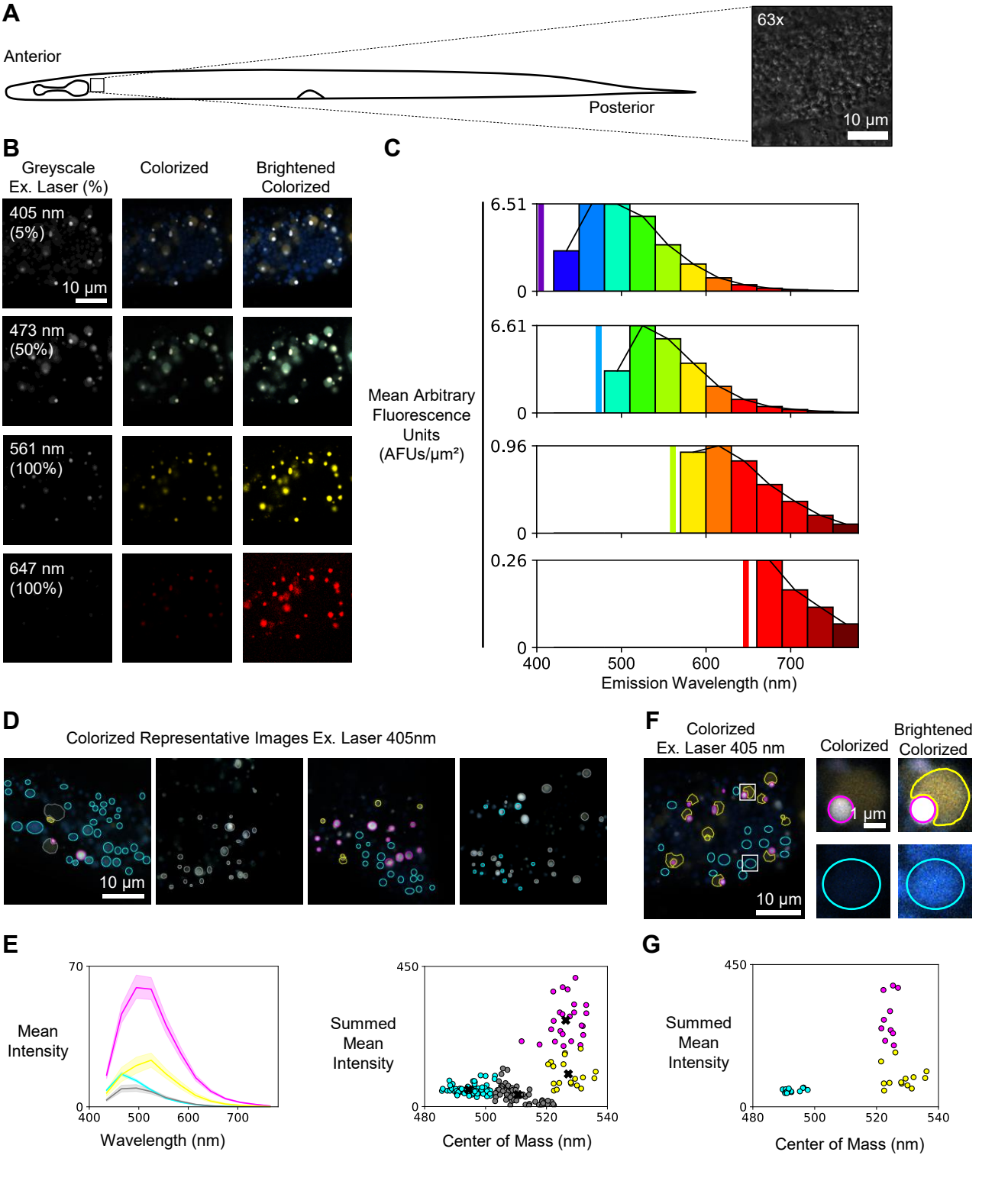
A
Anterior
Posterior
63x
10 µm
B
Greyscale
Ex. Laser (%)
Colorized
Brightened
Colorized
405 nm
(5%)
10 µm
473 nm
(50%)
561 nm
(100%)
647 nm
(100%)
C
Mean Arbitrary
Fluorescence
Units
(AFUs/µm²)
6.51
0
6.61
0
0.96
0
0.26
0
400
500
600
700
Emission Wavelength (nm)
D
Colorized Representative Images Ex. Laser 405nm
10 µm
F
Colorized
Ex. Laser 405 nm
Colorized
Brightened
Colorized
µm
10 µm
E
Mean
Intensity
70
0
400
500
600
700
Wavelength (nm)
Summed
Mean
Intensity
450
0
480
500
520
540
Center of Mass (nm)
G
Summed
Mean
Intensity
450
0
480
500
520
540
Center of Mass (nm)

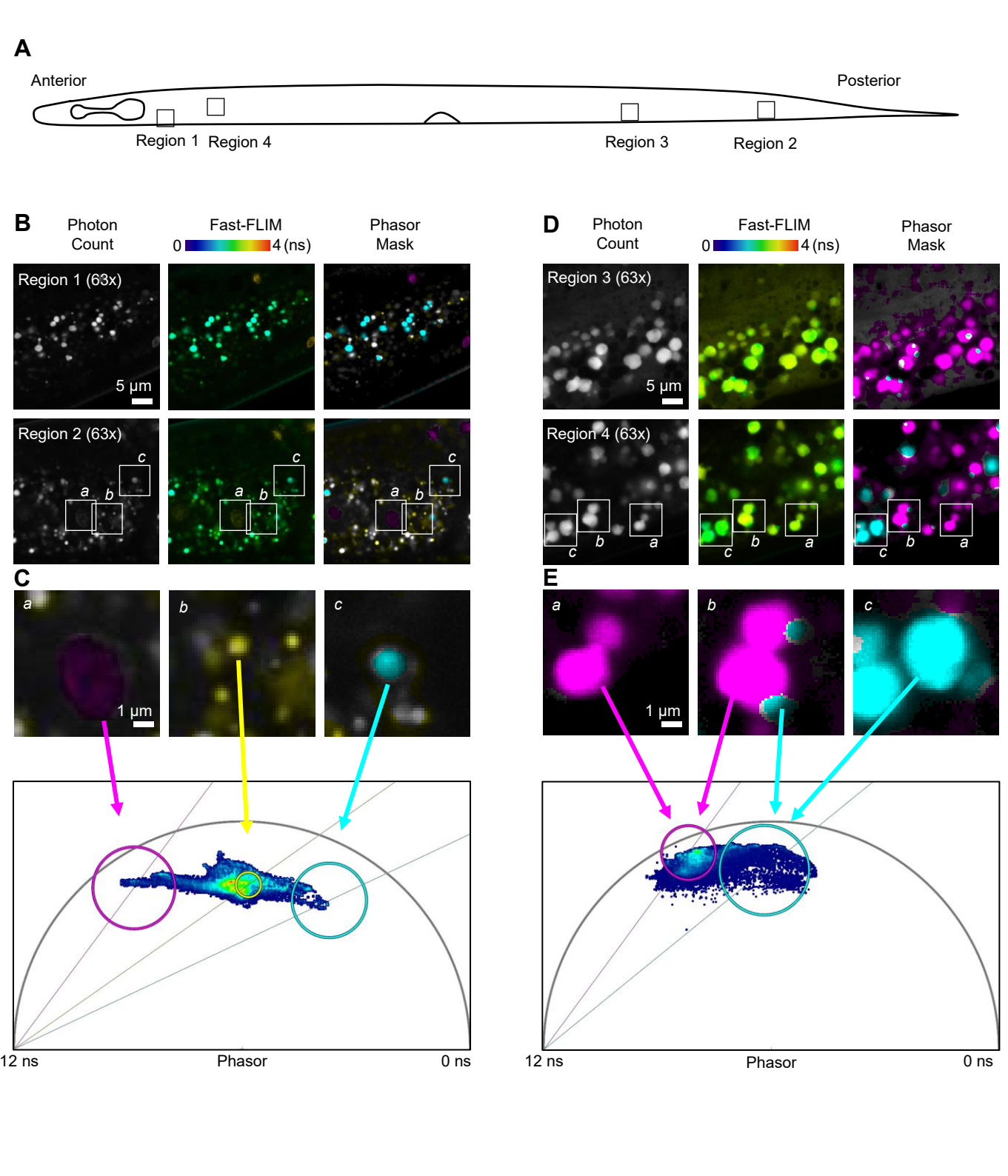
A
Anterior
Posterior
Region 1
Region 4
Region 3
Region 2
B
Photon Count
Fast-FLIM
0
4 (ns)
Phasor Mask
Region 1 (63x)
5 µm
Region 2 (63x)
a
b
c
C
1 µm
12 ns
Phasor
0 ns
D
Region 3 (63x)
Region 4 (63x)
E

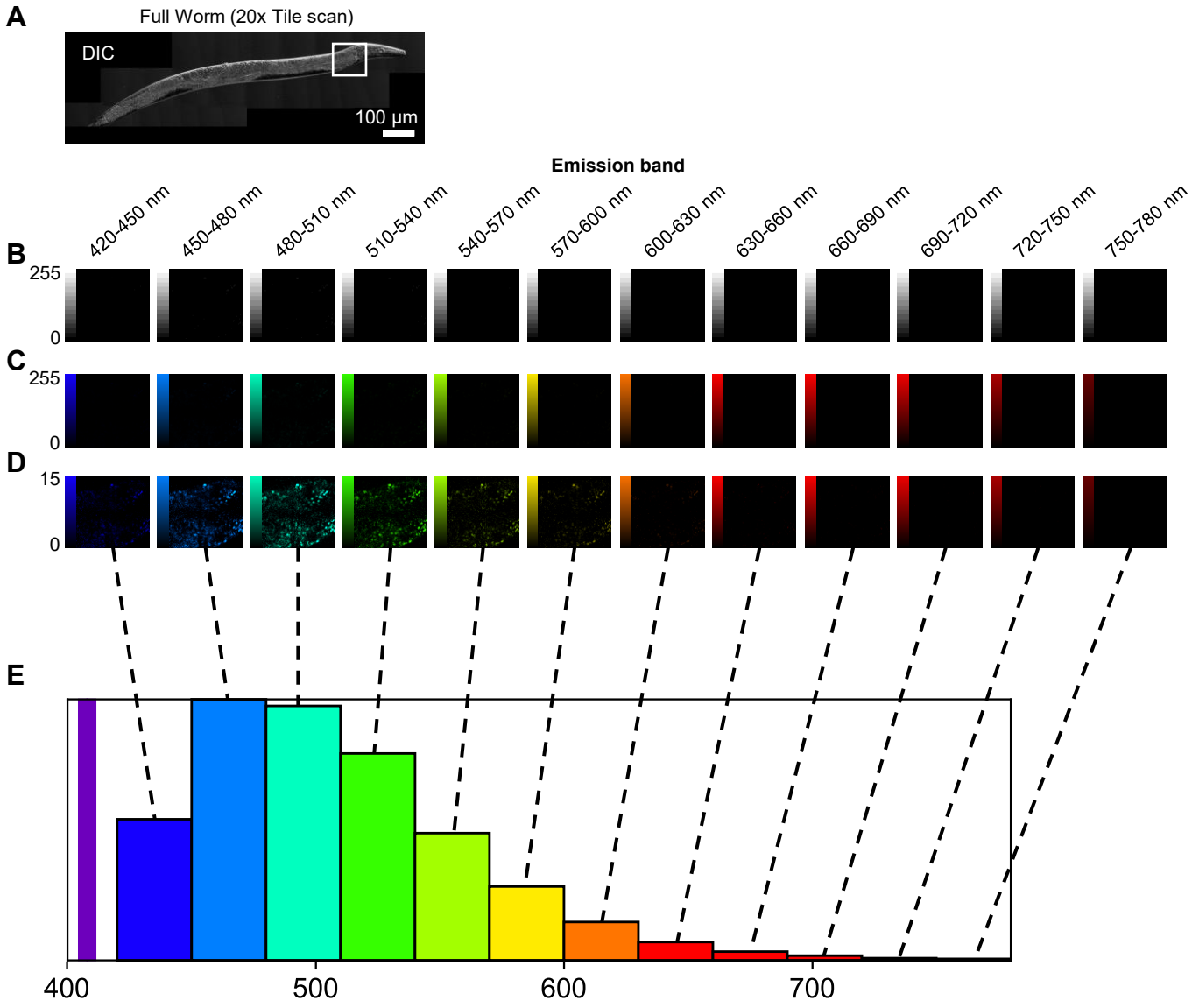
A
Full Worm (20x Tile scan)
DIC
100 µm
Emission band
420-450 nm
450-480 nm
480-510 nm
510-540 nm
540-570 nm
570-600 nm
600-630 nm
630-660 nm
660-690 nm
690-720 nm
720-750 nm
750-780 nm
B
255
0
C
255
0
D
15
0
E
400
500
600
700

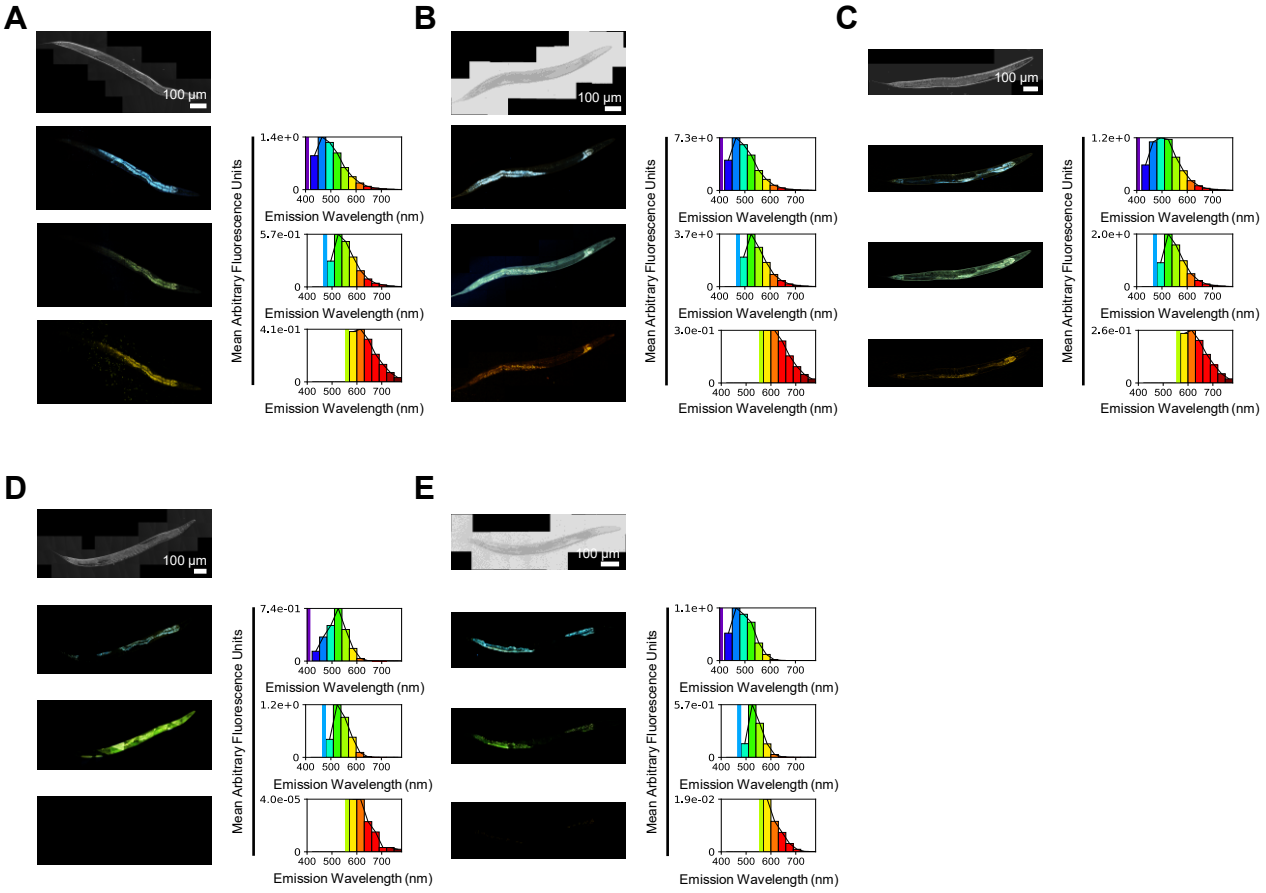
A
B
C
D
E
100 µm
Mean Arbitrary Fluorescence Units
Emission Wavelength (nm)
400 500 600 700
1.4e+0
0
5.7e-01
4.1e-01
7.3e+0
3.7e+0
3.0e-01
1.2e+0
2.0e+0
2.6e-01
7.4e-01
4.0e-05
1.1e+0
5.7e-01
1.9e-02

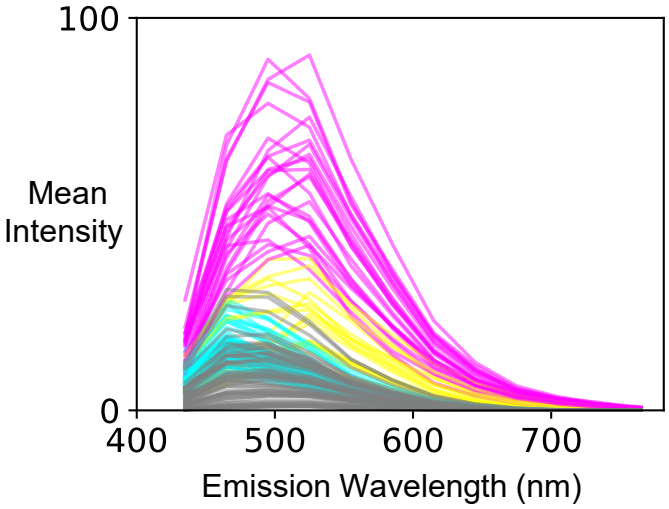
100
Mean
Intensity
0
400
500
600
700
Emission Wavelength (nm)

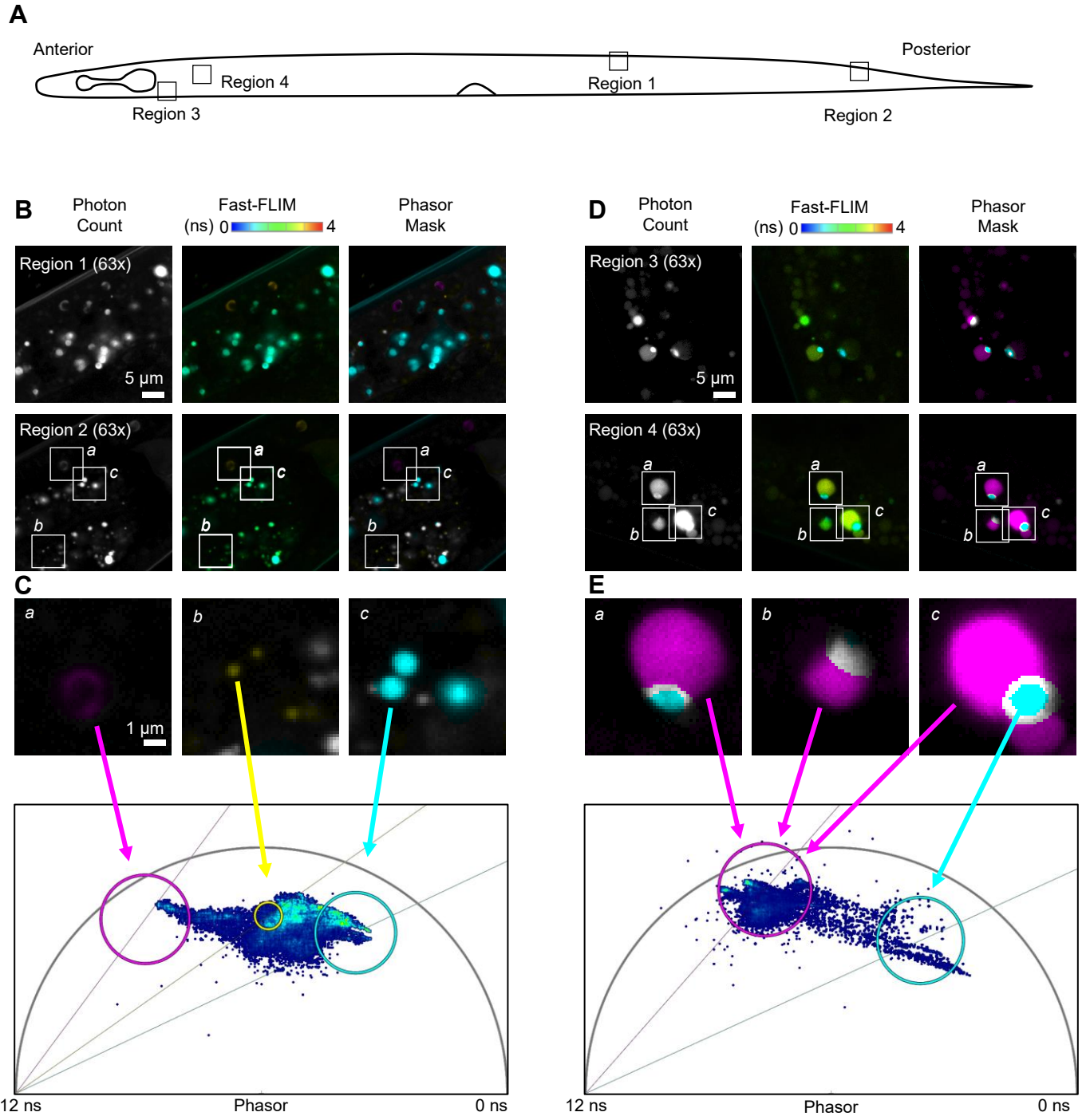
A
Anterior
Posterior
Region 4
Region 1
Region 3
Region 2
B
Photon Count
Fast-FLIM
(ns) 0
4
Phasor Mask
Region 1 (63x)
5 µm
Region 2 (63x)
a
b
c
C
1 µm
12 ns
Phasor
0 ns
D
Region 3 (63x)
Region 4 (63x)
E